Stability, electronic structures, and band alignment of two-dimensional II_A-IV-N_2 materials

Hong Ming Tang,* An-An Sun,* and Shang-Peng Gao†
Department of Materials Science, Fudan University, Shanghai 200433, People's Republic of China

(Received 1 June 2020; accepted 5 August 2020; published 25 August 2020)

Structural and phonon properties, formation and cohesive energies, and electronic structures of II_A-IV-N_2 (where II_A = Be or Mg; IV = Si, Ge, or Sn) monolayers with a graphenelike planar structure are systematically studied. Stability and property evolution with the variation of constituent group II_A and group IV elements are revealed. Dynamical and elastic stability of II_A-IV-N_2 monolayers is justified by phonon and elasticity calculations, respectively. Their wide band gaps ranging from 3.32 to 5.61 eV are predicted by the *GW* method on top of density functional calculations. The fat-band analysis and charge-density calculation of selected eigenstates unveil the effect of chemical environment and elemental substitution on electronic states near the band-gap region. The quasi-free-electron state and the parabolic dispersion of the lowest conduction band are advantageous for electron transport in electronic applications. A close examination of the band alignment and structural similarity between monolayers of II_A-IV-N_2 compounds and III nitrides indicates that it is possible to form type-I or type-II heterostructures and alloy systems composed of monolayers of II_A-IV-N_2 compounds and III nitrides. The findings in this work will promote research aiming at the synthesis, characterization, and application of novel two-dimensional materials, alloys, and heterostructures.

DOI: 10.1103/PhysRevMaterials.4.084004

I. INTRODUCTION

As ternary analogs of group III nitrides, the II-IV-N_2 materials are derived from replacing four group III atoms bonded to each nitrogen atom in the wurtzite structure by two group II and two group IV atoms [1,2]. This replacement leads to a wurtzite-derived orthorhombic structure (space group $Pna2_1$, No. 33), which has been found experimentally for $ZnSiN_2$, $ZnGeN_2$, $ZnSnN_2$, $BeSiN_2$, $MgSiN_2$, and $MgGeN_2$ (see Ref. [2] for a history of the development of these II-IV-N_2 materials until 2013) and has been reported theoretically but not experimentally verified for $BeGeN_2$ [3,4], $MgSnN_2$ [5,6], and Cd-IV-N_2 (IV = Si, Ge, or Sn) [7].

Similar to group III nitrides, the II-IV-N_2 materials are of significant interest for their optoelectronic applications, either to complement or to replace group III nitrides. To date, the most extensively studied of these materials is $ZnGeN_2$ [2,8–12], which is well lattice matched to and has a band gap (3.4 eV [11]) close to that of wurtzite GaN, making it suitable for use in optoelectronic and other wide-band-gap-semiconductor-based devices [6,8]. $ZnSnN_2$ has also received considerable attention for solar cell applications in that it is composed of earth-abundant elements and has a relatively low band gap (∼1.7 eV) [13–15]. For other II-IV-N_2 compounds, $MgSiN_2$ and $MgGeN_2$, for instance, are expected to have wider band gaps and are thus promising for use in short-wavelength optoelectronics [6,16,17]. Close lattice matching between II-IV-N_2 compounds ($ZnGeN_2$, $MgSiN_2$, $MgGeN_2$, etc.) and wurtzite III nitrides (GaN and AlN) has been found [12,16,18,19], suggesting the possibility of growing the heterostructures or alloys between them, without significant strain. The use of $MgSiN_2$ [20,21] as host lattices for phosphors activated by rare-earth ions such as Eu^{2+} and Ce^{3+} has been extensively studied, exhibiting compelling luminescence properties. Besides these optoelectronic applications, II-Si-N_2 (II = Be or Mg) compounds have gained some attention as high-temperature ceramics with reasonable mechanical properties [22–24]. $MgSiN_2$ is also widely used as a sintering additive for Si_3N_4 ceramics [25–27] and has been identified as a potential anode coating for Mg batteries [28].

The dimensionality reduction from three- to two-dimensional (2D) materials is expected to create a wide range of novel properties and phenomena. In addition to extensively studied 2D single-element materials (such as graphene and silicene) and 2D binary materials (such as monolayer and few-layer structures of transition-metal dichalcogenides [29], BN [30], AlN [31], and GaN [32]), two representatives of 2D ternary materials are hexagonal BCN (h-BCN) [33] and transition-metal dichalcogenide ternary alloys [34]. The 2D h-BCN atomic layers are of interest for band engineering and for use in electronics such as field-effect transistors to realize a good on/off ratio and high carrier mobility [35]. The 2D transition-metal dichalcogenide ternary alloys such as $Mo_xW_{1-x}S_2$ and $MoS_{2x}Se_{2(1-x)}$ monolayers [34] have tunable band gaps and are important for photovoltaic [36], electrocatalytic [37], and other optoelectronic [38,39] applications.

However, to date, there are only a few theoretical studies on 2D II-IV-N_2 ternary compounds based on density functional theory (DFT). Fang *et al.* [40] proposed a graphenelike planar structure for monolayer $ZnSnN_2$ and a reconstructed structure for bilayer $ZnSnN_2$. The former monolayer structure was also predicted to be stable for Zn-IV-N_2 [41,42] (IV = Si, Ge, or

*These authors contributed equally to this work.
†Corresponding author: gaosp@fudan.edu.cn

Sn) and Cd-IV-N_2 (IV = Si or Ge) [42] compounds. Their stability, electronic structures, optical properties, and potential use as photocatalysts for water splitting have been explored [40–42]. Inspired by these previous studies concerning II_B-IV-N_2 2D materials composed of group II_B elements Zn or Cd, in this work we perform a first-principles study of the monolayer structures of II_A-IV-N_2 (II_A = group II_A elements Be or Mg; IV = Si, Ge, or Sn) compounds. This substitution of group II_A for II_B elements is expected to expand the II-IV-N_2 family and to widen the range of accessible properties. We examine the geometric structures of II_A-IV-N_2 monolayers in detail. The stability of II_A-IV-N_2 monolayers is evaluated by their cohesive energies, formation energies, elastic tensors, and phonon dispersions. Additionally, we calculate the electronic structures of II_A-IV-N_2 monolayers using both the DFT and *GW* methods. The orbital character of their electronic states is also examined by the fat-band projection and charge-density calculation of selected bands. In view of the aforementioned close lattice matching between bulk II-IV-N_2 compounds and group III nitrides, their monolayer counterparts are expected to exhibit similar characteristics. Accordingly, we investigate the band alignment and lattice constants of monolayers of II_A-IV-N_2 compounds and III nitrides, discuss the possibility of forming the heterostructures or alloys consisting of II_A-IV-N_2 and III-nitride monolayers, and identify the type of corresponding heterostructure.

II. COMPUTATIONAL METHODS

Most of our calculations are performed using the abinit package [43]. The generalized gradient approximation (GGA) of the Perdew-Burke-Ernzerhof (PBE) form [44] is used for the exchange-correlation functional of DFT. The energy cutoff of the plane-wave basis set is set to 35 hartree (952.4 eV). A Monkhorst-Pack $6 \times 6 \times 1$ $\boldsymbol{k}$-point grid is chosen for monolayer structures. To avoid spurious interactions between adjacent monolayers, a vacuum of 15 Å is introduced along the direction perpendicular to monolayers. In the geometry optimization, the projector augmented-wave potential [45,46] is employed and the following electrons are treated as valence electrons: Be ($1s^2 2s^2$), Mg ($2s^2 2p^6 3s^2$), Si ($3s^2 3p^2$), Ge ($3d^{10} 4s^2 4p^2$), Sn ($4d^{10} 5s^2 5p^2$), and N ($2s^2 2p^3$). The Broyden-Fletcher-Goldfarb-Shanno scheme and a maximal absolute force tolerance of 5×10^{-6} hartree/bohr are adopted. The semiempirical van der Waals correction scheme proposed by Grimme [47,48] is employed in geometry optimization. For monolayers of $MgSiN_2$ and $MgSnN_2$, a fat-band analysis, in which the projected weights of Bloch states onto *s*, *p*, and *d* orbitals are obtained, along with the charge-density calculation of selected bands, serves to examine the orbital character of their electronic states. Elastic constants, which are the second derivatives of total energy with respect to two strain components, are obtained from density functional perturbation theory (DFPT) [49].

The *GW* method following the standard one-shot G_0W_0 approach [50] is used to improve the prediction of band energies. Kohn-Sham energies and orbitals obtained from DFT GGA calculations using the norm-conserving pseudopotential are used as input for the evaluation of *GW* self-energy correction. The equilibrium structures obtained from DFT GGA calculations are adopted in *GW* calculations. The plasmon-pole approximation [51] is used for the evaluation of the screened Coulomb interaction. The dielectric matrix has a cutoff energy of 15 hartree (408 eV). The numbers of bands used in the calculations of the screening and self-energy matrices are set to 150. The Coulomb truncation method [52] is used in *GW* calculations to remove image interactions which would otherwise hinder the convergence. The band edge positions are calculated with respect to the vacuum level, which is determined by averaging the electrostatic potential in the planes parallel to the monolayer plane in DFT GGA calculations. Then the *GW* band edge positions are obtained from the DFT GGA band edges and *GW* correction.

The castep code [53] is used to calculate phonon dispersions based on DFPT [54–56]. Here we use on-the-fly-generated norm-conserving pseudopotentials and PBE GGA. An energy cutoff of 1360 eV and a Monkhorst-Pack $7 \times 7 \times 1$ $\boldsymbol{k}$-point grid are chosen.

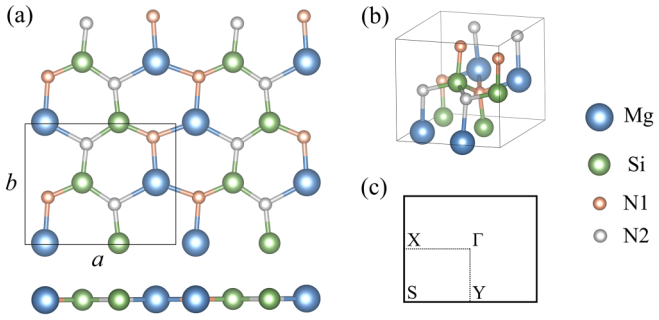

FIG. 1. Schematic illustration of (a) monolayer and (b) bulk structures of II_A-IV-N_2 compounds. The images shown are drawn using the structural parameters of $MgSiN_2$ under equilibrium conditions. There are two inequivalent N sites, labeled N1 and N2, indicating their different chemical environments. (c) Brillouin zone of II_A-IV-N_2 monolayers with high-symmetry points labeled.

III. RESULTS AND DISCUSSION

A. Structures of II_A-IV-N_2 monolayers

The initial structures for II_A-IV-N_2 monolayers can be derived from the elemental substitution in binary hexagonal monolayers (e.g., BN) or from the cleavage along the (001) plane from their respective bulk wurtzite-derived orthorhombic structures. The initial monolayer structure transforms into a graphenelike planar structure (space group $Pb2_1m$, No. 26) after geometry optimization, as has been predicted for II_B-IV-N_2 (II_B = Zn or Cd; IV = Si, Ge, or Sn) monolayers [40–42].

The bulk and monolayer structures of II_A-IV-N_2 compounds are shown in Fig. 1. The lattice constants *a* and *b*, lattice constant ratios b/a, and atomic reduced coordinates of six II_A-IV-N_2 monolayers are listed in Table I. No published results are available for comparison. A unit cell of II_A-IV-N_2 monolayers contains eight atoms. The lattice constants increase as the IV element changes from Si to Ge to Sn. For the ideal hexagonal structure, the lattice constant ratio b/a is $\sqrt{3}/2$ and all bond lengths are equal. Thus, the deviation of II_A-IV-N_2 monolayer structures from the hexagonal structure can be evaluated by the ratio b/a and the differences

TABLE I. Lattice constants a and b, lattice constant ratios b/a, and reduced coordinates of II_A-IV-N_2 (II_A = Be or Mg; IV = Si, Ge, or Sn) monolayers. The lattice constant ratio b/a is used as an indicator of the deviation of the orthorhombic monolayer structures from the hexagonal structure, which is $\sqrt{3}/2$ for the latter.

Compounds	Lattice constants			Reduced coordinates
	a (Å)	b (Å)	b/a	
$BeSiN_2$	5.725	4.953	0.865	Be (0.120,0.025), Si (0.635,0.017), N1 (0.119,0.351), N2 (0.625,0.357)
$BeGeN_2$	5.911	5.126	0.867	Be (0.119,0.025), Ge (0.642,0.017), N1 (0.105,0.341), N2 (0.635,0.368)
$BeSnN_2$	6.258	5.392	0.862	Be (0.119,0.021), Sn (0.659,0.019), N1 (0.079,0.321), N2 (0.642,0.389)
$MgSiN_2$	6.568	5.246	0.799	Mg (0.132,0.015), Si (0.621,0.012), N1 (0.151,0.391), N2 (0.593,0.333)
$MgGeN_2$	6.701	5.528	0.825	Mg (0.126,0.021), Ge (0.623,0.011), N1 (0.143,0.377), N2 (0.610,0.341)
$MgSnN_2$	6.957	5.953	0.856	Mg (0.122,0.024), Sn (0.631,0.015), N1 (0.124,0.356), N2 (0.625,0.355)

between bond lengths. In Table I the ratios b/a of II_A-IV-N_2 monolayers are smaller than $\sqrt{3}/2$ for all cases, similar to those of bulk II_A-IV-N_2 materials [7], except for $BeGeN_2$, whose b/a is slightly larger. The II_A-IV-N_2 monolayer structures therefore deviate to different extents from the hexagonal structure, arising from the different bond lengths of II_A-N and IV-N bonds. The ratios b/a for monolayer $BeSiN_2$ and $BeGeN_2$ are very close to $\sqrt{3}/2$, suggesting that they are very close to the hexagonal structure. The Mg-IV-N_2 (IV = Si, Ge, or Sn) monolayers, whose values of b/a deviate more from $\sqrt{3}/2$, are more distorted from the hexagonal structure, which may be attributed to the large atomic radius of Mg.

For trigonally bonded II_A-IV-N_2 monolayers, there are two inequivalent nitrogen sites denoted by N1 and N2, as shown in Fig. 1. The N1 site, depicted in red, is surrounded by one IV and two II_A atoms and the N2 in gray by one II_A and two IV atoms. For each of the II_A-IV-N_2 monolayers, the lengths of four types of bonds (IV-N1, IV-N2, II_A-N1, and II_A-N2) are shown in Fig. 2. For the ideal hexagonal structure (e.g., graphene and hexagonal BN), all bond lengths are equal. Thus, the length difference of different types of bonds in II_A-IV-N_2 monolayers is another indicator of the deviation from the hexagonal structure, in addition to the ratio b/a. In Fig. 2, the length differences between II_A-N and IV-N bonds are fairly large, for $MgSiN_2$ in particular, consistent with the aforementioned large distortion of monolayer $MgSiN_2$ from the hexagonal structure. Monolayer $BeSiN_2$, with the ratio b/a closest to $\sqrt{3}/2$ (see Table I) and nearly equal lengths of II_A-N and IV-N bonds, is closest to the hexagonal structure, arising from the relative similarity in the atomic radius and electronegativity between elements Be and Si.

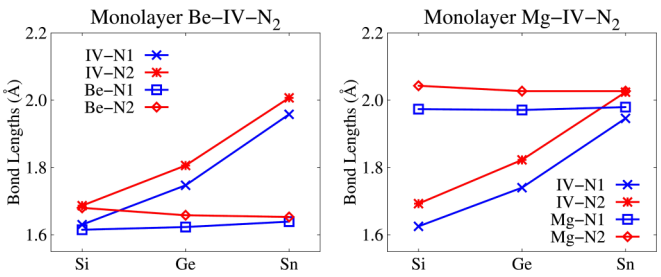

FIG. 2. Variation of bond lengths between different II_A-IV-N_2 (II_A = Be or Mg; IV = Si, Ge, or Sn) monolayers. The lengths of IV- and II_A-N1 bonds and of IV- and II_A-N2 bonds are depicted in blue and red, respectively.

Figure 2 shows that the length differences between II_A-N and IV-N bonds increase (decrease) for Be-IV-N_2 (Mg-IV-N_2) monolayers as the IV element changes from Si to Ge to Sn, consistent with the variation in the radius differences between II_A and IV atoms on going from Si to Ge to Sn. The lengths of both IV-N1 and IV-N2 bonds increase from Si to Ge to Sn due to the increasing atomic radius and the weakening of bonding. The larger atomic radius of Mg also leads to longer Mg-N bonds than Be-N ones. In contrast, the lengths of both II_A-N1 and II_A-N2 bonds remain nearly unchanged on going from Si to Ge to Sn, except for small fluctuations, as is also true for IV-N1 and IV-N2 bonds on going from Be to Mg. Moreover, each of the II_A-IV-N_2 monolayers has longer II_A(IV)-N2 bonds than II_A(IV)-N1 ones, due to the different chemical environments of N1 and N2 atoms.

B. Dynamical, elastic, and energetic stability

As stated in Refs. [57,58], a crystalline structure is stable, under no external load, and in the harmonic approximation, if and only if it has dynamical stability (i.e., all its phonon modes have positive frequencies for all wave vectors) and elastic stability (i.e., its elastic energy is always positive). To examine the dynamical stability of II_A-IV-N_2 monolayers, their phonon dispersions and phonon density of states are calculated and shown in Fig. 3. We note that as the atomic mass of II_A and IV elements increases the phonon modes become softer in general, similar to the case of bulk II-IV-N_2 compounds [19]. The Be-IV-N_2 and Mg-IV-N_2 monolayers are dynamically stable in that there are no imaginary frequencies in their phonon spectra. Our calculation indicates that Ca-IV-N_2 monolayers with similar planar structures are dynamically unstable (not shown here). The stability of the slightly deformed honeycomb flat monolayer does not guarantee the stability of the bulk crystals formed by stacking of these monolayers. In the case of binary GaN, monolayer GaN is dynamically stable, whereas bulk h-GaN is dynamically unstable and will evolve into another crystal structure in molecular dynamics simulation [59]. The hexagonal bulk crystals composed of planar II-IV-N_2 monolayers are unlikely to exist. The stability of multilayer II-IV-N_2 structures requires further investigation.

The highest phonon frequency decreases as the IV element changes from Si to Ge to Sn due to the increasing mass of the IV element, as well as the decreasing bond strength which is reflected in the increase in IV-N bond lengths, as mentioned in the case of bulk II-IV-N_2 compounds [60]. The phonon

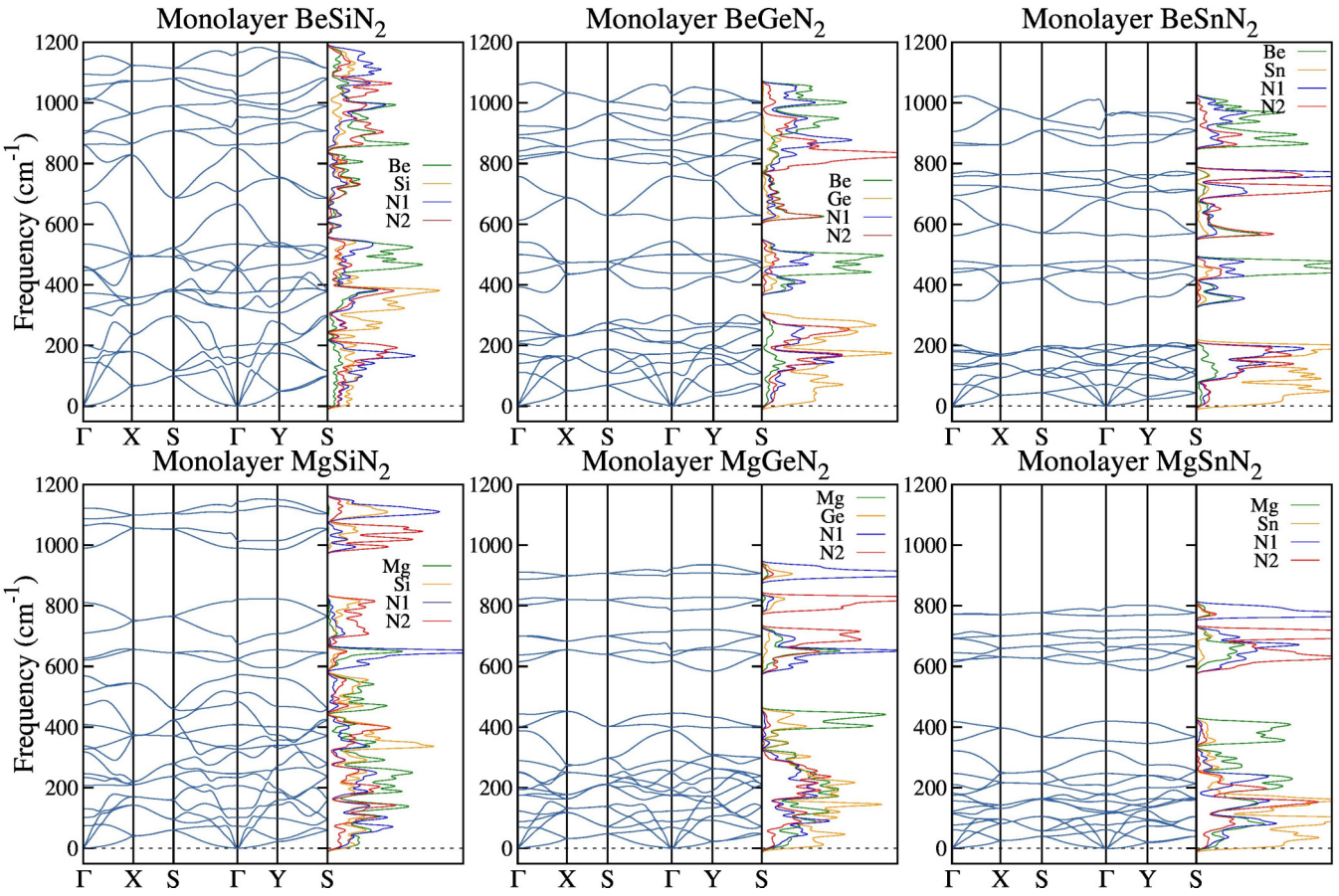

FIG. 3. Phonon dispersion and phonon density of states of II_A-IV-N_2 (II_A = Be or Mg; IV = Si, Ge, or Sn) monolayers. The dotted line indicates the position of zero values.

spectrum of $BeSiN_2$ exhibits a large dispersion and no distinct gap is found, because of the relatively small mass differences between constituent atoms. In contrast, there are one or more gaps in the phonon spectra of other II_A-IV-N_2 monolayers. For example, a large gap appears in the phonon spectra of $MgSiN_2$ between 823 and 985 cm^{-1}. For $BeGeN_2$, there are two phonon gaps between 543 and 613 cm^{-1} and between 300 and 384 cm^{-1}.

In order to elucidate elastic stability, the elastic constants of II_A-IV-N_2 monolayers have been calculated by DFPT. Elastic constants C_{ijkl} ($i, j, k, l = 1, 2, 3$ for 3D or $i, j, k, l = 1, 2$ for 2D materials) are the proportionality between stress σ_{ij} and imposed strain ε_{kl}:

$$\sigma_{ij} = C_{ijkl}\varepsilon_{kl}, \tag{1}$$

where C_{ijkl} can be written as a fourth-rank tensor $\mathbf{C}$. It is a 6×6 matrix [Eq. (2)] for 3D materials in nontensorial Voigt notation:

$$\mathbf{C} = \begin{bmatrix} C_{1111} & C_{1122} & C_{1133} & C_{1123} & C_{1131} & C_{1112} \\ C_{1122} & C_{2222} & C_{2233} & C_{2223} & C_{2231} & C_{2212} \\ C_{1133} & C_{2233} & C_{3333} & C_{3323} & C_{3331} & C_{3312} \\ C_{1123} & C_{2223} & C_{3323} & C_{2323} & C_{2331} & C_{2312} \\ C_{1131} & C_{2231} & C_{3331} & C_{2331} & C_{3131} & C_{3112} \\ C_{1112} & C_{2212} & C_{3312} & C_{2312} & C_{3112} & C_{1212} \end{bmatrix}. \tag{2}$$

The matrix elements in Eq. (1) can be obtained directly from elasticity calculations using many popular *ab initio* codes. For 2D materials (taking the z axis perpendicular to the 2D plane), the matrix elements C_{ijkl} will be zero when any of i, j, k, l is 3, and the Voigt notation is reduced to a 3×3 matrix [Eq. (3)] for 2D materials:

$$\mathbf{C} = \begin{bmatrix} C_{1111} & C_{1122} & C_{1112} \\ C_{1122} & C_{2222} & C_{2212} \\ C_{1112} & C_{2212} & C_{1212} \end{bmatrix}. \tag{3}$$

However, different from the typical Voigt notation defined above, a second-rank tensor notation (Mandel notation) [Eq. (4)] can be adopted for elastic tensors in the definition of elastic stability criteria for 2D materials, according to Ref. [58]:

$$\mathbf{C} = \begin{bmatrix} C_{1111} & C_{1122} & \sqrt{2}C_{1112} \\ C_{1122} & C_{2222} & \sqrt{2}C_{2212} \\ \sqrt{2}C_{1112} & \sqrt{2}C_{2212} & 2C_{1212} \end{bmatrix} = \begin{bmatrix} C_{11} & C_{12} & C_{13} \\ C_{12} & C_{22} & C_{23} \\ C_{13} & C_{23} & C_{33} \end{bmatrix}. \tag{4}$$

If the 3×3 matrix in the second-rank tensor notation shown in Eq. (4) is positive definite, then the corresponding 2D material is elastically stable. For II_A-IV-N_2 monolayers with a rectangular lattice, where C_{13} and C_{23} are zero, the elastic stability criteria for the second-rank tensor matrix in Eq. (4) to be positive definite become $C_{11} > 0$, $C_{33} > 0$, and $C_{11}C_{22} > C_{12}^2$ [58]. The elastic tensors for II_A-IV-N_2 monolayers, of which four nonzero components are C_{11}, C_{22}, C_{12}, and C_{33}, are listed in Table II. It is clear that II_A-IV-N_2 monolayers

TABLE II. Elastic constants C_{ij} (in units of 100 GPa) in the second-rank tensor notation (Mandel notation) [58] for II_A-IV-N_2 (II_A = Be or Mg; IV = Si, Ge, or Sn) monolayers. Note that for the present symmetry, the difference between the Mandel notation and the typical Voigt one (in parentheses) is only a factor of 2 for C_{33}.

Components	$BeSiN_2$	$BeGeN_2$	$BeSnN_2$	$MgSiN_2$	$MgGeN_2$	$MgSnN_2$
C_{11} (C_{1111})	1.05	0.98	0.80	0.81	0.71	0.59
C_{22} (C_{2222})	1.13	1.00	0.78	0.67	0.63	0.58
C_{12} (C_{1122})	0.37	0.34	0.32	0.42	0.38	0.33
C_{33} ($2C_{1212}$)	0.72	0.64	0.48	0.54	0.43	0.29

are elastically stable since their elastic constants fulfill the criteria. The elastic constants become smaller as the II and IV atomic numbers increase, except that C_{12} increases from Be to Mg.

The energetic stability of bulk and monolayer II_A-IV-N_2 structures can be evaluated by their cohesive (E_{coh}) and formation (E_f) energies. The cohesive energy (per atom) E_{coh} is given by

$$E_{coh} = \frac{n_{II_A}E_{II_A} + n_{IV}E_{IV} + n_N E_N - E_{total}}{n_{II_A} + n_{IV} + n_N}, \quad (5)$$

where n_{II_A}, n_{IV}, and n_N are the numbers of II_A, IV, and N atoms per unit cell; E_{II_A}, E_{IV}, and E_N are the energies of an isolated atom of II_A, IV, and N elements, respectively; and E_{total} is the total energy per unit cell of bulk and monolayer II_A-IV-N_2 compounds. For the isolated atoms B, N, Si, Ge, and Sn, spin polarization is taken into account. The formation energy (per formula unit) E_f of bulk and monolayer II_A-IV-N_2 compounds from constituent elements, whose stable structures are chosen as the reference systems, is defined as

$$E_f = \frac{E_{total}}{n_{formula}} - E(II_A) - E(IV) - E(N_2), \quad (6)$$

where $E(II_A)$ is the energy per atom of Be or Mg in the hexagonal-close-packed structure; $E(IV)$ is the energy per atom of Si, Ge, or Sn in the diamond structure; $E(N_2)$ is the energy of a N_2 gas molecule; and $n_{formula}$ is the number of formula units per unit cell, two for the monolayer and four for bulk II_A-IV-N_2 structures. We also calculate the formation energy E_f' of II_A-IV-N_2 monolayers with respect to graphenelike Be_3N_2 or Mg_3N_2 monolayers, which are predicted by DFT in Refs. [61,62]. It is given by

$$E_f' = \frac{E_{total}}{n_{formula}} - \frac{E(II_3N_2)}{3} - E(IV) - \frac{2}{3}E(N_2), \quad (7)$$

where $E(II_3N_2)$ is the energy per formula unit of monolayer Be_3N_2 or Mg_3N_2.

Figures 4 and 5 illustrate the cohesive and formation energies of bulk and monolayer II_A-IV-N_2 compounds. Note that the higher the cohesive energy and the lower the formation energy, the greater the stability of II_A-IV-N_2 compounds. As shown in Fig. 4, good agreement can be found between the previously reported values and our calculated cohesive energies, validating our computational scheme. The cohesive energies of bulk and monolayer II_A-IV-N_2 compounds are both comparable to or higher than those of their Si, Ge, and Sn counterparts, though lower than BN ones, suggesting the

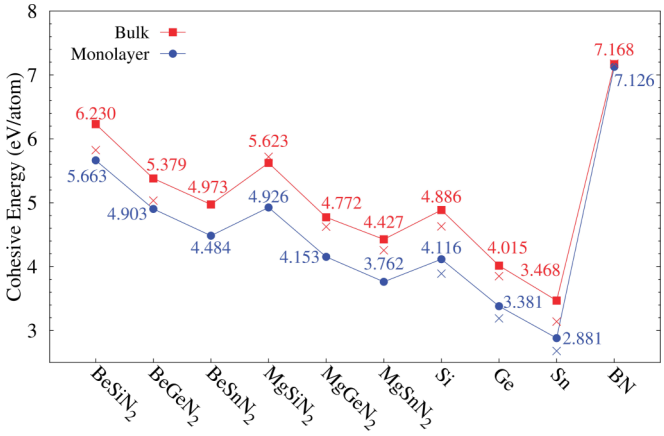

FIG. 4. Cohesive energies per atom E_{coh} of bulk (red) and monolayer (blue) II_A-IV-N_2 (II_A = Be or Mg; IV = Si, Ge, or Sn) structures. For comparison, the cohesive energies of bulk and monolayer structures of Si, Ge, Sn (i.e., their diamond structures, silicene, germanene, and stanene), and BN (i.e., wurtzite BN and graphenelike monolayer BN) are also shown. Values of bulk structures taken from Refs. [4,6,63,64] are shown by red crosses. Values of silicene, germanene, and stanene taken from Ref. [65] are shown by blue crosses.

energetic stability of bulk and monolayer II_A-IV-N_2 compounds. Figure 5 shows that most of II_A-IV-N_2 monolayers, which have negative E_f (or E_f'), are more stable compared with II_A and IV elements in their stable structures at ambient conditions and N_2 molecules (or II_3N_2 monolayers, bulk IV structures, and N_2 molecules). Two II_A-Si-N_2 (II_A = Be or Mg) monolayers have the lowest formation energies and are most promising for experimental studies, while two II_A-Sn-N_2 monolayers have positive formation energies and may be unstable. For Be-IV-N_2 monolayers $E_f < E_f'$, while for Mg-IV-N_2 ones the opposite is true. This is consistent with

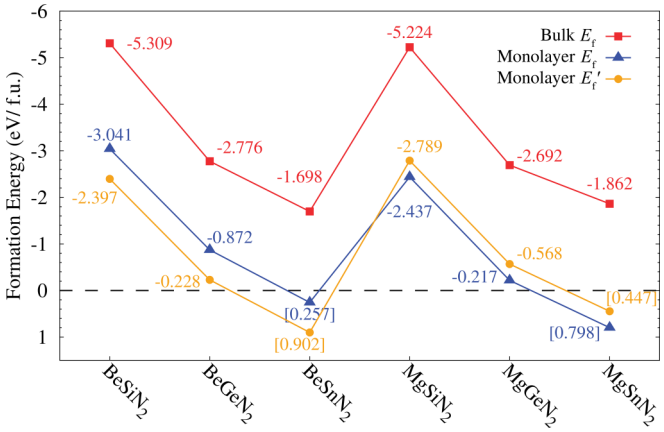

FIG. 5. Formation energies per formula unit of bulk (red) and monolayer (blue or yellow) II_A-IV-N_2 (II_A = Be or Mg; IV = Si, Ge, or Sn) structures. The E_f (or E_f') are calculated with respect to bulk II_A and IV structures and N_2 molecules (or II_3N_2 monolayers, bulk IV structures, and N_2 molecules). The black dashed line marks the position of zero energy. Positive energy values are given in square brackets.

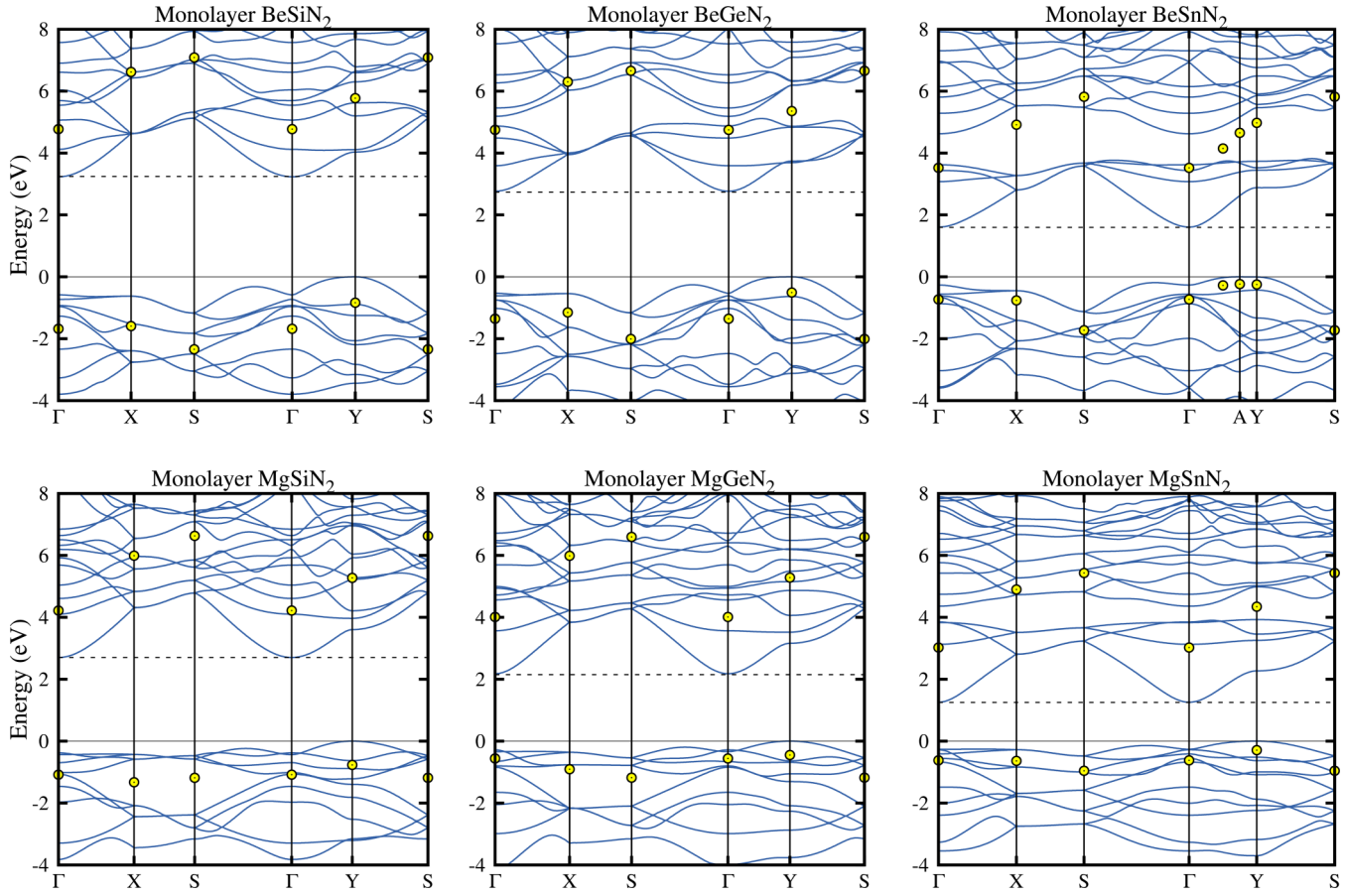

FIG. 6. Band structures of II_A-IV-N_2 (II_A = Be or Mg; IV = Si, Ge, or Sn) monolayers. Blue curves are dispersion curves calculated by DFT GGA and yellow circles indicate *GW*-corrected energies at high-symmetry points for the highest valence and lowest conduction bands. In each panel, a dashed line indicates the location of the CBM and a solid line the VBM.

monolayer Be_3N_2's lower and Mg_3N_2's higher energy than their respective bulk II_A structures and N_2 molecules, as indicated by our calculations and Refs. [61,62]. Moreover, the formation energies of II_A-IV-N_2 monolayers from their bulk materials can be obtained from the data in Fig. 4, by subtracting the cohesive energies of monolayers from those of corresponding bulk materials, which are in the range of 0.47–0.70 eV/atom for II_A-IV-N_2 monolayers. These values are all comparable to the formation energies of monolayer silicene (0.77 eV/atom), germanene (0.634 eV/atom), and stanene (0.587 eV/atom) obtained in this work and in Ref. [65] (0.65, 0.48, and 0.44 eV/atom for silicene, germanene, and stanene, respectively), demonstrating the energetic stability of II_A-IV-N_2 monolayers.

The variations of E_{coh} and E_f between different compounds share certain similarities. First, II_A-IV-N_2 monolayers have slightly lower E_{coh} and higher E_f than corresponding bulk phases, which is common for 2D materials and their bulk counterparts. Additionally, the E_{coh} drops and E_f rises as the IV element changes from Si to Ge to Sn, due to the weakening of bonding as addressed above. Interestingly, each of the Be-IV-N_2 structures has slightly higher E_{coh} and lower E_f than its Mg-IV-N_2 counterpart. It is thus possible that, in the freestanding case, Be-IV-N_2 monolayers are slightly more stable relative to Mg-IV-N_2 ones.

C. Electronic structures and *GW* band energies

The electronic structures of II_A-IV-N_2 monolayers are calculated using DFT GGA. Due to the well-known underestimation of band gaps in DFT calculations, the *GW* calculations on top of DFT GGA results are performed to improve the accuracy of band-gap prediction. The band structures of six II_A-IV-N_2 (II_A = Be or Mg; IV = Si, Ge, or Sn) monolayers are shown in Fig. 6. The GGA results show that six II_A-IV-N_2 monolayers all have indirect band gaps slightly lower than the direct gap at the Γ point, with the conduction-band minimum (CBM) at Γ and the valance-band maximum (VBM) at Y, except for monolayer $BeSnN_2$ whose VBM is located at (−0.375,0,0) (labeled A) between Γ and Y. Both direct and indirect energy gaps calculated by the GGA and *GW* methods are listed and compared in Table III. It is clear in Fig. 6 that the *GW*-corrected energy gaps at high-symmetry points are considerably larger than the GGA ones. The GGA and *GW* calculations yield the same band-gap type (indirect). As expected, the band gaps of II_A-IV-N_2 monolayers become narrower as the atomic numbers of II_A and IV elements increase, due to the weakening of bonding with increasing atomic radii. This trend is typical for group IV, II-VI, and III-V semiconductors. Additionally, we note that II_A-IV-N_2 (II_A = Be or Mg; IV = Si, Ge, or Sn) monolayers have considerably larger band gaps (ranging from 1.256 to

TABLE III. Energy gaps (in eV) of II_A-IV-N_2 (II_A = Be or Mg; IV = Si, Ge, or Sn) monolayers calculated by the DFT GGA and *GW* methods. Since the highest valence band energies at Y and Γ are quite close, both indirect ($Y \rightarrow \Gamma$ if not indicated otherwise) and direct energy gaps ($\Gamma \rightarrow \Gamma$) are listed. The minimum band gaps are shown in bold.

	DFT GGA		*GW*	
Monolayers	Indirect	Direct	Indirect	Direct
$BeSiN_2$	**3.232**	3.815	**5.606**	6.451
$BeGeN_2$	**2.767**	3.298	**5.258**	5.929
$BeSnN_2$	**1.607 ($A \rightarrow \Gamma$)**	1.872	**3.755 ($A \rightarrow \Gamma$)**	4.250
$MgSiN_2$	**2.701**	3.080	**4.988**	5.303
$MgGeN_2$	**2.178**	2.462	**4.460**	4.572
$MgSnN_2$	**1.256**	1.520	**3.318**	3.333

3.232 eV from DFT GGA calculations) than those of II_B-IV-N_2 (II_B = Zn or Cd; IV = Si, Ge, or Sn) monolayers (ranging from 0.292 to 2.564 eV from DFT GGA calculations; see Ref. [42] for their band-gap values). The former is expected to extend the application of II-IV-N_2 monolayers to the deeper ultraviolet region.

Furthermore, we examine the orbital character of the electronic states of II_A-IV-N_2 monolayers. We focus on monolayer $MgSiN_2$ and $MgGeN_2$ in particular, whose bulk counterparts have been successfully synthesized and aroused considerable research interest. Figure 7 shows the fat-band representation and projected density of states (PDOS) of monolayer $MgSiN_2$ and $MgGeN_2$, offering two complementary perspectives in revealing the orbital character. The electronic states of these two monolayers have some similarities but also clear distinctions. Their valence bands are both dominated by the N1 p and N2 p states. However, the conduction bands have more Si (or Ge) character and the PDOS does not add up to the total density of states due to the fact that delocalized conduction band states cannot be effectively expanded in terms of a limited number of atomiclike basis functions. The VBM has mainly N1 p and N2 p but also minor Mg d and IV d character. The minor d

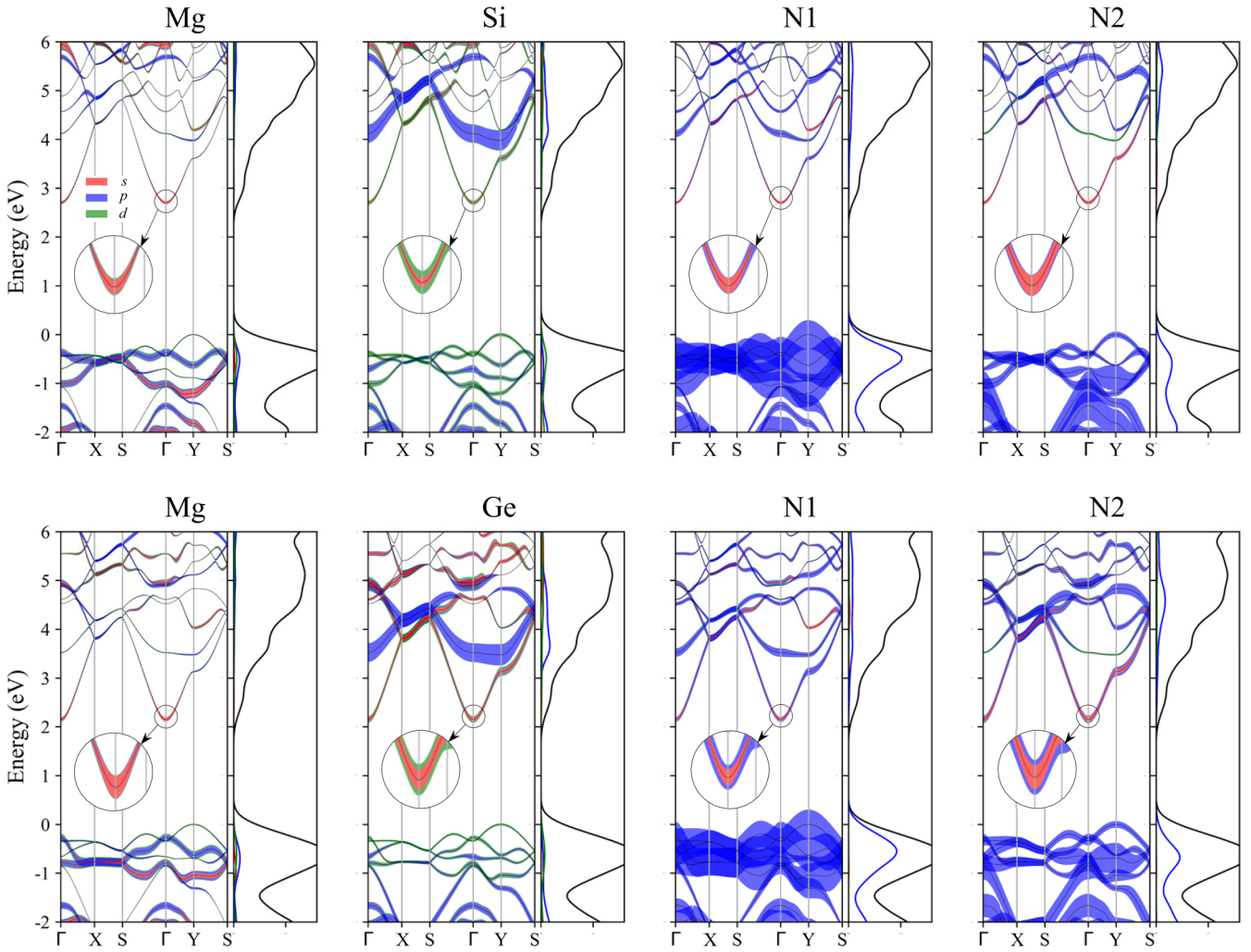

FIG. 7. Projected band structures and density of states of monolayer $MgSiN_2$ (top panels) and $MgGeN_2$ (bottom panels). The stripe widths correspond to the projected weights of Bloch states onto different atomic orbitals (red for s, blue for p, and green for d). The projected density of states and projected weights, summed over all equivalent atoms in the unit cell, i.e., over two Mg, two Si (or Ge), two N1, and two N2 atoms, are shown in four panels for $MgSiN_2$ (or $MgGeN_2$). The VBM at Y is located at zero energy.

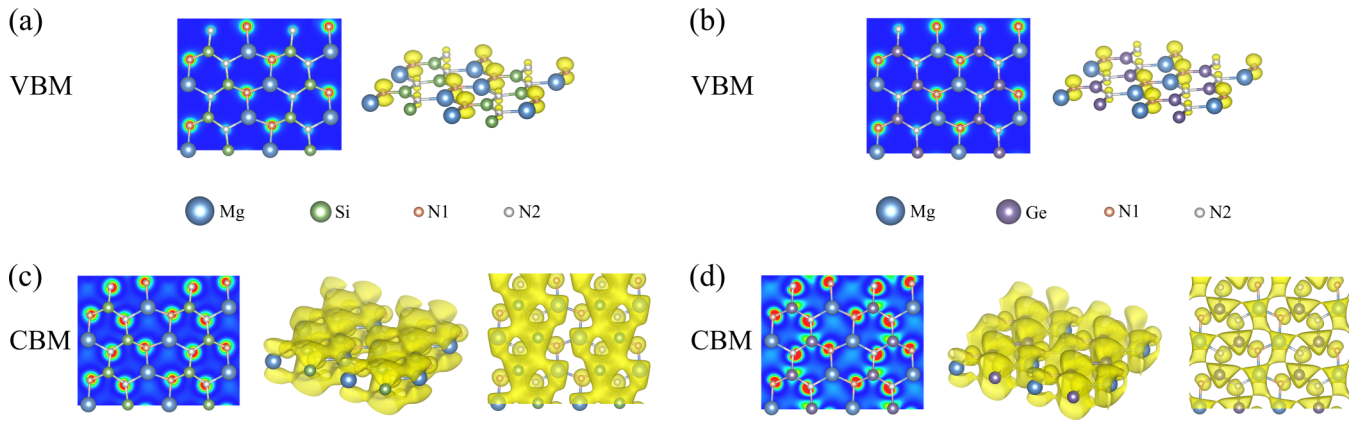

FIG. 8. Single-state charge densities of (a) and (b) the VBM and (c) and (d) the CBM of (a) and (c) $MgSiN_2$ and (b) and (d) $MgGeN_2$ monolayers. Both 2D maps in the atomic plane and 3D isosurfaces of charge densities are displayed. The saturation levels shown for 2D maps are between 0 (blue) and 0.005 $e/Å^3$ (red) for the VBM and 0 (blue) and 0.05 $e/Å^3$ (red) for the CBM. The isosurface values are 0.05 $e/Å^3$ for the VBM and 0.005 $e/Å^3$ for the CBM.

character appearing in valence bands is the result of orbital mixing and charge redistribution when forming crystals. The N1 p states contribute more than the N2 p states near the VBM whereas the N2 contribution is slightly more important to states near the CBM, demonstrating the appreciable effect of chemical environment on electronic states, i.e., the N1 atom can attract more valence electrons from its two Mg neighbors and thus leave less empty orbitals compared to the N2 atom, which is bonded with one Mg and two IV atoms. The charge densities of VBM and CBM states are plotted in Fig. 8. For the VBM charge densities of $MgSiN_2$ and $MgGeN_2$ [Figs. 8(a) and 8(b)], the dumbbell-shaped p orbitals of N1 and N2 atoms are recognized. The N1 and N2 atoms are easy to distinguish in Fig. 8, by a larger N1 contribution than N2 for the VBM and the other way round for the CBM.

The CBM has mainly Mg s, N1 s, N2 s, IV s, and IV d character, to which four types of inequivalent atoms contribute nearly equally, as can be observed from their similar stripe widths in Fig. 7. The highly dispersive conduction band indicates low electron effective mass, which is always beneficial for the transportation of photoexcited electrons. Similar characteristics have also been observed in the PDOS of bulk Mg-IV-N_2 [6] and monolayer Zn-IV-N_2 [42] compounds. Our calculated effective masses for II_A-IV-N_2 monolayers, evaluated through a parabolic fit to the conduction band dispersion curves, are listed in Table IV.

TABLE IV. Calculated electron effective masses (in units of free-electron mass m_e) along the ΓS and ΓY directions for II_A-IV-N_2 (II_A = Be or Mg; IV = Si, Ge, or Sn) monolayers.

Compounds	$m_{\Gamma S}$	$m_{\Gamma Y}$
$BeSiN_2$	0.715	0.727
$BeGeN_2$	0.529	0.470
$BeSnN_2$	0.404	0.311
$MgSiN_2$	0.539	0.566
$MgGeN_2$	0.356	0.402
$MgSnN_2$	0.266	0.290

They are in the range of $0.2m_e$–$0.8m_e$ for both the ΓS and ΓY directions, which is comparable to the effective masses of common semiconductors (e.g., Si, Ge, GaN, and AlN). The effective masses become smaller as the II and IV atomic numbers increase, corresponding to lower CBM states in energy and larger conduction band dispersion. For the CBM electron densities of both $MgSiN_2$ and $MgGeN_2$ illustrated in Figs. 8(c) and 8(d), while there are localized distributions around N1 and N2 atoms, electrons spreading over the large interstitial region above and below the monolayer (near Mg and Si/Ge atoms) can be observed, indicating the nearly-free-electron nature of the lowest-lying conduction band, which is consistent with the parabolic dispersion of this band. The delocalized electronic states near the CBM are similar to those observed in monolayer AlN [66] and can be taken as a more localized analog of the free-electron states in graphene, graphite, and h-BN [67,68].

Compared with monolayer $MgSiN_2$, an increased amount of the N1 and N2 contributions near the band-gap region is observed in monolayer $MgGeN_2$. The N2 increase is slightly larger than N1, since the substitution of IV elements has a larger effect on the N2 atoms (bonded to two IV atoms) than on N1 (bonded to one IV atom). Moreover, while the CBM of $MgSiN_2$ has more IV d than IV s character, the opposite is the case for $MgGeN_2$. In other words, the IV s character of the CBM becomes increasingly noticeable as we go from Si to Ge. The conduction bands near the CBM of $MgGeN_2$, several of which have sizable Ge p character, are found to drop in energy well below those of $MgSiN_2$, corresponding to the smaller band gap of $MgGeN_2$ and the lower-lying Ge s and Ge p levels. For the CBM [Figs. 8(c) and 8(d)], we also find that electrons are overall more localized in $MgGeN_2$ than in $MgSiN_2$, forming capsule-shaped isosurfaces around Ge atoms, consistent with the larger PDOS at the CBM for all four inequivalent sites in $MgGeN_2$ (Fig. 7).

D. Band alignment

As mentioned above, many of the bulk II-IV-N_2 compounds ($ZnGeN_2$, $MgSiN_2$, $MgGeN_2$, etc.) are closely lattice

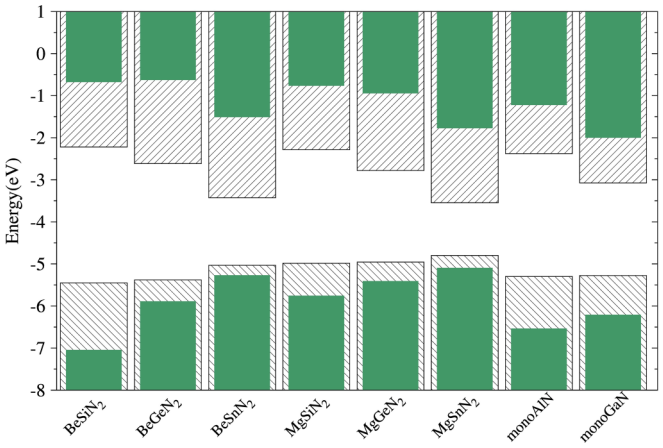

FIG. 9. Band alignment of II_A-IV-N_2 (II_A = Be or Mg; IV = Si, Ge, or Sn), GaN and AlN monolayers. The band-edge energies (VBM and CBM) calculated by the DFT GGA (shaded bars) and *GW* approach (green bars) are shown with respect to the vacuum energies, which are obtained from the electronic potential distribution in the supercell.

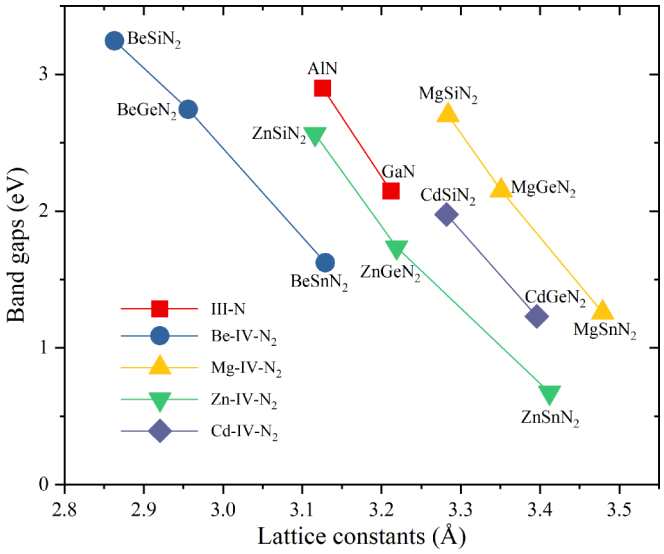

FIG. 10. Band gaps (calculated by DFT GGA) as a function of lattice constants for III-N and II-IV-N_2 monolayers. Here the lattice constants shown are the average hexagonal-like lattice constant $\bar{a}_h = (a/2 + b/\sqrt{3})/2$ for II-IV-N_2 monolayers (where a and b are the lattice constants of their orthorhombic structures) and the hexagonal lattice constants for III-N monolayers. The values of Zn-IV-N_2 and Cd-IV-N_2 monolayers are taken from Ref. [42]. The $CdSnN_2$ monolayer is not shown due to its dynamical instability.

matched to wurtzite III nitrides (GaN and AlN) and thus might be readily alloyed with them, or grown with them in heterostructures, without significant strain [12,16,18,19]. We therefore anticipate that similar conclusions will hold for II_A-IV-N_2 and III-N monolayers. It is worth noting that monolayers of GaN and AlN have a graphenelike planar structure as shown by DFT calculations [69], and the ultrathin films of AlN (submonolayer to 12 monolayers) have been successfully grown on Ag (111) single crystals [31]. These important achievements render monolayer III nitrides promising for use in 2D optoelectronics. Özçelik *et al.* studied band alignment of elemental and binary monolayer semiconductors using DFT calculations [70]. To explore the possibility of forming the heterostructures or alloys composed of II_A-IV-N_2 and III-N monolayers, we calculate their lattice constants, along with their band alignment, to predict the type of the heterostructures. Figure 9 shows the band alignment of II_A-IV-N_2 (II_A = Be or Mg; IV = Si, Ge, or Sn) and III-N monolayers, in which both the GGA and *GW* results are shown. Our following analysis is based on the *GW* results.

For Be-IV-N_2 and Mg-IV-N_2 monolayers, the VBM increases as the IV element changes from Si to Ge to Sn, similar to the trend in lattice constants while different from the variation of the CBM. The *GW*-corrected CBM of the $BeSiN_2$ monolayer lies slightly below that of the $BeGeN_2$ monolayer, exhibiting a different trend from the GGA results. For monolayers containing the same IV atom (Si, Ge, or Sn), Mg-IV-N_2 monolayers have a higher VBM and lower CBM than Be-IV-N_2 ones. Moreover, we find that monolayer AlN has the second lowest VBM (higher than that of monolayer $BeSiN_2$) and its CBM is higher than those of monolayer $BeSnN_2$ and $MgSnN_2$. Monolayer AlN acts as a narrow-band-gap semiconductor when forming type-I heterostructures with monolayer $BeSiN_2$, or as a wide-band-gap semiconductor when forming type-I heterostructures with monolayer $BeSnN_2$ and $MgSnN_2$. Combining monolayer AlN and the remaining II_A-IV-N_2 monolayers would make type-II heterostructures. According to *GW* band edges, monolayer GaN can be combined with monolayer $BeSiN_2$ to form type-I heterostructures and with the remaining II_A-IV-N_2 monolayers to form type-II heterostructures.

We note that monolayer GaN (or AlN) has a hexagonal structure while II-IV-N_2 monolayers have a distorted hexagonal one. Thus, an average hexagonal-like lattice constant $\bar{a}_h = (a/2 + b/\sqrt{3})/2$ can be defined for II-IV-N_2 monolayers, where a and b are the lattice constants of their orthorhombic structures. The $\bar{a}_h$ can be compared with the hexagonal lattice constant of III-N monolayers, as displayed in Fig. 10. Note that the close lattice match between III-N and II-IV-N_2 monolayers requires both similar lattice constants and small deviation of the latter from the hexagonal structure. We find that monolayer AlN (GaN) is closely lattice matched to monolayers of $BeSnN_2$ and $ZnSiN_2$ ($MgSiN_2$, $CdSiN_2$, and $ZnGeN_2$), suggesting the possibility of growing the epitaxial heterostructures (lateral or vertical) between them, without significant strain. In addition, it is possible to tune the strain by choosing different II_A-IV-N_2 monolayers to form heterostructures with monolayer AlN (or GaN). For instance, monolayer AlN is under tensile (compressive) strain when grown with monolayer $MgSiN_2$ ($BeGeN_2$) to form heterostructures. It is also possible that the alloying of different II_A-IV-N_2 monolayers with each other will create a situation where the lattice mismatch with monolayer GaN (or AlN) vanishes, which will be very advantageous when considering the epitaxial growth of 2D heterostructures. Band-gap tuning of the alloy systems should also be possible, via alloying II_A-IV-N_2 monolayers with each other and with GaN and AlN monolayers, as is the case with bulk II-IV-N_2 materials [16,18,71].

IV. CONCLUSION

Planar monolayer structures for II_A-IV-N_2 (II_A = Be or Mg; IV = Si, Ge, or Sn) compounds are proposed and the dynamical and elastic stability of these structures is confirmed by phonon and elasticity calculations. This monolayer structure is slightly distorted from the graphenelike hexagonal structure and can be derived from the elemental substitution in binary hexagonal monolayers and subsequent structural relaxation. It can also be regarded as obtained by the relaxation of initial puckered monolayers cleaved from bulk orthorhombic II_A-IV-N_2 compounds. Comparable in cohesive energies with typical elemental and binary monolayers, the ternary II_A-IV-N_2 monolayers are energetically stable, among which II_A-Si-N_2 monolayers with the lowest formation energies are most promising for experimental studies, whereas II_A-Sn-N_2 monolayers have positive formation energies and may be unstable. The monolayers of six II_A-IV-N_2 compounds have band gaps ranging from 3.32 to 5.61 eV based on *GW* calculations, rendering them promising for short-wavelength optoelectronic applications. A detailed examination of the electronic states of monolayers $MgSiN_2$ and $MgGeN_2$ has revealed distinctly different orbital character for the electronic states near the VBM and CBM. The highly dispersive conduction bands and low electron effective mass of II_A-IV-N_2 monolayers will enable high mobility of photoexcited electrons and are advantageous for electronic applications. Moreover, as is the case with bulk materials, we find that type-I or type-II heterostructures may be grown between II_A-IV-N_2 and III-N monolayers based on their band alignment. For those II-IV-N_2 monolayers (or their alloys) closely lattice matched to III-N monolayers, it is possible to grow the epitaxial heterostructures (lateral or vertical) between them. It is also possible to tune the strain by selecting different II_A-IV-N_2 monolayers (or their alloys) to form heterostructures with III-N monolayers. Alloying II_A-IV-N_2 monolayers with each other and with III-N monolayers should also enable band-gap tuning of the alloy systems. The II_A-IV-N_2 monolayers are expected to be of interest for electronic and optoelectronic applications to complement the nitride semiconductor family.

ACKNOWLEDGMENTS

This work was supported by the Natural Science Foundation of Shanghai (Grant No. 19ZR1404300) and the Innovation Program of Shanghai Municipal Education Commission (Grant No. 15ZZ001).

[1] A. D. Martinez, A. N. Fioretti, E. S. Toberer, and A. C. Tamboli, J. Mater. Chem. A **5**, 11418 (2017).
[2] W. R. L. Lambrecht and A. Punya, in *III-Nitride Semiconductors and their Modern Devices*, edited by B. Gill (Oxford University Press, Oxford, 2013), Chap. 15, pp. 519–585.
[3] V. Shaposhnikov, A. Krivosheeva, F. Arnaud D'Avitaya, J. L. Lazzari, and V. Borisenko, Phys. Status Solidi B **245**, 142 (2008).
[4] S. Lyu and W. R. L. Lambrecht, J. Phys.: Condens. Matter **31**, 335501 (2019).
[5] M. Råsander and M. A. Moram, J. Phys. D **51**, 375101 (2018).
[6] A. P. Jaroenjittichai and W. R. L. Lambrecht, Phys. Rev. B **94**, 125201 (2016).
[7] S. Lyu and W. R. L. Lambrecht, Phys. Rev. Mater. **1**, 024606 (2017).
[8] L. Han, C. Lieberman, and H. Zhao, J. Appl. Phys. **121**, 093101 (2017).
[9] A. Punya, W. R. L. Lambrecht, and M. van Schilfgaarde, Phys. Rev. B **84**, 165204 (2011).
[10] A. Punya and W. R. L. Lambrecht, Phys. Rev. B **88**, 075302 (2013).
[11] K. Du, C. Bekele, C. C. Hayman, J. C. Angus, P. Pirouz, and K. Kash, J. Cryst. Growth **310**, 1057 (2008).
[12] L. Han, K. Kash, and H. Zhao, J. Appl. Phys. **120**, 103102 (2016).
[13] P. C. Quayle, K. He, J. Shan, and K. Kash, MRS Commun. **3**, 135 (2013).
[14] L. Lahourcade, N. C. Coronel, K. T. Delaney, S. K. Shukla, N. A. Spaldin, and H. A. Atwater, Adv. Mater. **25**, 2562 (2013).
[15] A. Zakutayev, J. Mater. Chem. A **4**, 6742 (2016).
[16] J. B. Quirk, M. Råsander, C. M. McGilvery, R. Palgrave, and M. A. Moram, Appl. Phys. Lett. **105**, 112108 (2014).
[17] M. Råsander and M. A. Moram, Mater. Res. Express **3**, 085902 (2016).
[18] B. H. D. Jayatunga, S. Lyu, S. K. Radha, K. Kash, and W. R. L. Lambrecht, Phys. Rev. Mater. **2**, 114602 (2018).
[19] M. Råsander, J. B. Quirk, T. Wang, S. Mathew, R. Davies, R. G. Palgrave, and M. A. Moram, J. Appl. Phys. **122**, 085705 (2017).
[20] C. J. Duan, A. C. A. Delsing, and H. T. Hintzen, J. Lumin. **129**, 645 (2009).
[21] V. Bondar, L. Axelrud, V. Davydov, and T. Felter, MRS Proc. **639**, G11.36 (2000).
[22] W. A. Groen and M. J. Kraan, J. Mater. Sci. **29**, 3161 (1994).
[23] D. J. Kaczynski, in *Kirk-Othmer Encyclopedia of Chemical Technology*, edited by K. Othmer (Wiley, New York, 2011).
[24] R. J. Bruls, A. A. Kudyba-Jansen, P. Gerharts, H. T. Hintzen, and R. Metselaar, J. Mater. Sci. Mater. Electron. **13**, 63 (2002).
[25] G. H. Peng, G. J. Jiang, W. L. Li, B. L. Zhang, and L. D. Chen, J. Am. Ceram. Soc. **89**, 3824 (2006).
[26] X. W. Zhu, Y. Sakka, Y. Zhou, and K. Hirao, J. Ceram. Soc. Jpn. **116**, 706 (2008).
[27] G. Peng, G. Jiang, H. Zhuang, W. Li, and S. Xu, Mater. Res. Bull. **40**, 2139 (2005).
[28] T. Chen, G. Sai Gautam, and P. Canepa, Chem. Mater. **31**, 8087 (2019).
[29] Q. H. Wang, K. Kalantar-Zadeh, A. Kis, J. N. Coleman, and M. S. Strano, Nat. Nanotechnol. **7**, 699 (2012).
[30] G. Cassabois, P. Valvin, and B. Gil, Nat. Photon. **10**, 262 (2016).
[31] P. Tsipas, S. Kassavetis, D. Tsoutsou, E. Xenogiannopoulou, E. Golias, S. A. Giamini, C. Grazianetti, D. Chiappe, A. Molle, M. Fanciulli, and A. Dimoulas, Appl. Phys. Lett. **103**, 251605 (2013).
[32] Z. Y. Al Balushi, K. Wang, R. K. Ghosh, R. A. Vilá, S. M. Eichfeld, J. D. Caldwell, X. Qin, Y.-C. Lin, P. A. DeSario,

G. Stone, S. Subramanian, D. F. Paul, R. M. Wallace, S. Datta, J. M. Redwing, and J. A. Robinson, Nat. Mater. **15**, 1166 (2016).
[33] J. Lu, S.-P. Gao, and J. Yuan, Ultramicroscopy **112**, 61 (2012).
[34] Q. Zeng, H. Wang, W. Fu, Y. Gong, W. Zhou, P. M. Ajayan, J. Lou, and Z. Liu, Small **11**, 1868 (2015).
[35] Y. Gong, G. Shi, Z. Zhang, W. Zhou, J. Jung, W. Gao, L. Ma, Y. Yang, S. Yang, G. You, R. Vajtai, Q. Xu, A. H. MacDonald, B. I. Yakobson, J. Lou, Z. Liu, and P. M. Ajayan, Nat. Commun. **5**, 3193 (2014).
[36] C. Li, Q. Cao, F. Wang, Y. Xiao, Y. Li, J.-J. Delaunay, and H. Zhu, Chem. Soc. Rev. **47**, 4981 (2018).
[37] J. Xu, X. Li, W. Liu, Y. Sun, Z. Ju, T. Yao, C. Wang, H. Ju, J. Zhu, S. Wei, and Y. Xie, Angew. Chem. Int. Ed. **56**, 9121 (2017).
[38] J. Park, M. S. Kim, B. Park, S. H. Oh, S. Roy, J. Kim, and W. Choi, ACS Nano **12**, 6301 (2018).
[39] H. Li, X. Duan, X. Wu, X. Zhuang, H. Zhou, Q. Zhang, X. Zhu, W. Hu, P. Ren, P. Guo, L. Ma, X. Fan, X. Wang, J. Xu, A. Pan, and X. Duan, J. Am. Chem. Soc. **136**, 3756 (2014).
[40] D. Q. Fang, X. Chen, P. F. Gao, Y. Zhang, and S. L. Zhang, J. Phys. Chem. C **121**, 26063 (2017).
[41] Y. Bai, G. Luo, L. Meng, Q. Zhang, N. Xu, H. Zhang, X. Wu, F. Kong, and B. Wang, Phys. Chem. Chem. Phys. **20**, 14619 (2018).
[42] H. M. Tang and S.-P. Gao, Comput. Mater. Sci. **158**, 88 (2019).
[43] X. Gonze, F. Jollet, F. Abreu Araujo, D. Adams, B. Amadon, T. Applencourt, C. Audouze, J.-M. Beuken, J. Bieder, A. Bokhanchuk *et al.*, Comput. Phys. Commun. **205**, 106 (2016).
[44] J. P. Perdew, K. Burke, and M. Ernzerhof, Phys. Rev. Lett. **77**, 3865 (1996).
[45] F. Jollet, M. Torrent, and N. Holzwarth, Comput. Phys. Commun. **185**, 1246 (2014).
[46] M. Torrent, F. Jollet, F. Bottin, G. Zérah, and X. Gonze, Comput. Mater. Sci. **42**, 337 (2008).
[47] A. D. Becke and E. R. Johnson, J. Chem. Phys. **124**, 221101 (2006).
[48] B. Van Troeye, M. Torrent, and X. Gonze, Phys. Rev. B **93**, 144304 (2016).
[49] D. R. Hamann, X. Wu, K. M. Rabe, and D. Vanderbilt, Phys. Rev. B **71**, 035117 (2005).
[50] X. Gonze, G.-M. Rignanese, M. Verstraete, J.-M. Beuken, Y. Pouillon, R. Caracas, F. Jollet, M. Torrent, G. Zerah, M. Mikami *et al.*, Z. Kristallogr. Cryst. Mater. **220**, 558 (2005).
[51] R. W. Godby and R. J. Needs, Phys. Rev. Lett. **62**, 1169 (1989).
[52] S. Ismail-Beigi, Phys. Rev. B **73**, 233103 (2006).
[53] S. J. Clark, M. D. Segall, C. J. Pickard, P. J. Hasnip, M. I. J. Probert, K. Refson, and M. C. Payne, Z. Kristallogr. Cryst. Mater. **220**, 567 (2005).
[54] S. Baroni, S. De Gironcoli, A. Dal Corso, and P. Giannozzi, Rev. Mod. Phys. **73**, 515 (2001).
[55] K. Refson, P. R. Tulip, and S. J. Clark, Phys. Rev. B **73**, 155114 (2006).
[56] X. Gonze and C. Lee, Phys. Rev. B **55**, 10355 (1997).
[57] F. Mouhat and F.-X. Coudert, Phys. Rev. B **90**, 224104 (2014).
[58] M. Maździarz, 2D Mater. **6**, 048001 (2019).
[59] A. Sun, S.-P. Gao, and G. Gu, Phys. Rev. Mater. **3**, 104604 (2019).
[60] T. R. Paudel and W. R. L. Lambrecht, Phys. Rev. B **78**, 115204 (2008).
[61] S. Ullah, P. A. Denis, R. B. Capaz, and F. Sato, New J. Chem. **43**, 2933 (2019).
[62] P.-F. Liu, L. Zhou, T. Frauenheim, and L.-M. Wu, Phys. Chem. Chem. Phys. **18**, 30379 (2016).
[63] C. Kittel, *Introduction to Solid State Physics*, 8th ed. (Wiley, New York, 2005), p. 50.
[64] A. Janotti, S. H. Wei, and D. J. Singh, Phys. Rev. B **64**, 174107 (2001).
[65] F. Matusalem, M. Marques, L. K. Teles, and F. Bechstedt, Phys. Rev. B **92**, 045436 (2015).
[66] A.-A. Sun, S.-P. Gao, and G. Gu, Chem. Sci. **11**, 4340 (2020).
[67] A. Catellani, M. Posternak, A. Baldereschi, and A. J. Freeman, Phys. Rev. B **36**, 6105 (1987).
[68] M. Posternak, A. Baldereschi, A. J. Freeman, E. Wimmer, and M. Weinert, Phys. Rev. Lett. **50**, 761 (1983).
[69] H. Şahin, S. Cahangirov, M. Topsakal, E. Bekaroglu, E. Akturk, R. T. Senger, and S. Ciraci, Phys. Rev. B **80**, 155453 (2009).
[70] V. O. Özçelik, J. G. Azadani, C. Yang, S. J. Koester, and T. Low, Phys. Rev. B **94**, 035125 (2016).
[71] P. Narang, S. Chen, N. C. Coronel, S. Gul, J. Yano, L. W. Wang, N. S. Lewis, and H. A. Atwater, Adv. Mater. **26**, 1235 (2014).